AB Aur, a Rosetta stone for studies of planet formation. II. H2S detection and sulfur budget

P. Rivière-Marichalar, A. Fuente, G. Esplugues, V. Wakelam, R. Le Gal, C. Baruteau, A. Ribas, E. Macías, R. Neri, D. Navarro-Almaida

HAL Id: insu-03860308

https://hal-insu.archives-ouvertes.fr/insu-03860308

Submitted on 19 Nov 2022

AB Aur, a Rosetta stone for studies of planet formation

II. H₂S detection and sulfur budget

P. Rivière-Marichalar [1], A. Fuente[1], G. Esplugues[1], V. Wakelam[2], R. le Gal[3,4], C. Baruteau[5], A. Ribas[6],
E. Macías[6,7,8], R. Neri[9], and D. Navarro-Almaida[1]

[1] Observatorio Astronómico Nacional (OAN,IGN), Calle Alfonso XII, 3. 28014 Madrid, Spain
 e-mail: `p.riviere@oan.es`
[2] Laboratoire d'Astrophysique de Bordeaux, Univ. Bordeaux, CNRS, B18N, allée Geoffroy Saint-Hilaire, 33615 Pessac, France
[3] Univ. Grenoble Alpes, CNRS, Institut de Planétologie et d'Astrophysique de Grenoble (IPAG), 38000 Grenoble, France
[4] Institut de Radioastronomie Millimétrique (IRAM), 38406 Saint-Martin d'Hères, France
[5] CNRS / Institut de Recherche en Astrophysique et Planétologie, 14 avenue Edouard Belin, 31400 Toulouse, France
[6] European Southern Observatory (ESO), Alonso de Córdova 3107, Vitacura, Casilla 19001, Santiago de Chile, Chile
[7] Joint ALMA Observatory, Alonso de Córdova 3107, Vitacura, Santiago 763-0355, Chile
[8] European Southern Observatory, Karl-Schwarzschild-Str 2, 85748 Garching, Germany
[9] Institut de Radioastronomie Millimétrique, 300 rue de la Piscine, 38406 Saint-Martin d'Hères, France

ABSTRACT

Context. The sulfur abundance is poorly known in most environments. Yet, deriving the sulfur abundance is key to understanding the evolution of the chemistry from molecular clouds to planetary atmospheres. We present observations of H₂S $1_{10}-1_{01}$ at 168.763 GHz toward the Herbig Ae star AB Aur.
Aims. We aim to study the abundance of sulfuretted species toward AB Aur and to constrain how different species and phases contribute to the sulfur budget.
Methods. We present new NOrthern Extended Millimeter Array (NOEMA) interferometric observations of the continuum and H₂S $1_{10}-1_{01}$ line at 168.763 GHz toward AB Aur. We derived radial and azimuthal profiles and used them to compare the geometrical distribution of different species in the disk. Assuming local thermodynamical equilibrium (LTE), we derived column density and abundance maps for H₂S, and we further used `Nautilus` to produce a more detailed model of the chemical abundances at different heights over the mid-plane at a distance of $r = 200$ au.
Results. We have resolved H₂S emission in the AB Aur protoplanetary disk. The emission comes from a ring extending from 0.67″ (∼109 au) to 1.69″ (∼275 au). Assuming $T = 30$ K, $n_H = 10^9$ cm⁻³, and an ortho-to-para ratio of three, we derived a column density of $(2.3 \pm 0.5) \times 10^{13}$ cm⁻². Under simple assumptions, we derived an abundance of $(3.1 \pm 0.8) \times 10^{-10}$ with respect to H nuclei, which we compare with `Nautilus` models to deepen our understanding of the sulfur chemistry in protoplanetary disks. Chemical models indicate that H₂S is an important sulfur carrier in the solid and gas phase. We also find an important transition at a height of ∼12 au, where the sulfur budget moves from being dominated by ice species to being dominated by gas species.
Conclusions. We confirm that present-day models still struggle to simultaneously reproduce the observed column densities of the different sulfuretted species, and the observed abundances are still orders of magnitude away from the cosmic sulfur abundance. Studying sulfuretted species in detail in the different phases of the interstellar medium is key to solving the issue.

Key words. astrochemistry – ISM: abundances – ISM: molecules – stars: formation

1. Introduction

Protoplanetary disks (PPDS) are the birthplace of planets, implying that a planet's composition is, at least partially, inherited from the disk. The protoplanetary disk chemical composition, in turn, is inherited from the natal molecular cloud, but modified by the prevailing physical conditions of protoplanetary disks. To study the chemical complexity of planetary atmospheres, one must understand that of protoplanetary disks. A topic of major interest due to its possible implications for the emergence of life is the chemical evolution of molecules that carry the six key elements in organic chemistry: H, C, O, N, S, and P.

Sulfur is the tenth most abundant element in the Universe and plays a crucial role in biological systems. The abundance toward the Sun (Asplund et al. 2009, $S/H \sim 1.5 \times 10^{-5}$) agrees well with the value derived toward Orion B stars for example

($S/H \sim 1.4 \times 10^{-5}$, Daflon et al. 2009). However, its chemistry is poorly understood in interstellar environments, and sulfuretted molecules are not as abundant as expected in the interstellar medium (ISM). While sulfur abundance is close to the cosmic value in the diffuse ISM and photon-dominated regions (PDRs; Goicoechea et al. 2006; Howk et al. 2006; Goicoechea & Cuadrado 2021), it is strongly depleted in the dense molecular gas (>10^4 cm⁻³), where only 0.1% of the sulfur cosmic abundance is observed (Tieftrunk et al. 1994; Wakelam et al. 2004; Vastel et al. 2018). A study of the sulfur content in dense cores by Hily-Blant et al. (2022) provides evidence for a progressive depletion of sulfur with age, as well as with density for a given core. It is expected that most of the sulfur is then locked on the icy mantles of dust grains in dense cores (Millar & Herbst 1990; Ruffle et al. 1999; Vidal et al. 2017; Laas & Caselli 2019). However, only solid OCS has been

unambiguously detected on the ice mantles of these objects thanks to the strength of its infrared band (Geballe et al. 1985; Palumbo et al. 1995). Furthermore, SO_2 has also been tentatively detected (Boogert et al. 1997). Since only upper limits for the solid H_2S abundance could be derived thus far (Jiménez-Escobar & Muñoz Caro 2011) and since detection is hampered by the strong overlap between the 2558 cm^{-1} band and the methanol bands at 2530 and 2610 cm^{-1}, the main gas and solid phase sulfur reservoirs thus remain unknown.

Sulfur-bearing species have been widely detected in the Solar System. In comets, they are detected mostly in the form of H_2S and S_2 (Mumma & Charnley 2011). Hale Bopp showed a large variety of detections, including CS and SO (Boissier et al. 2007). Furthermore, CS was also detected toward the comets C/2012 F6 (Lemmon) and C/2014 Q2 (Lovejoy; Biver et al. 2016). Using the Rosetta Orbiter Spectrometer for Ion and Neutral Analysis (ROSINA; Balsiger et al. 2007) on board Rosetta, H_2S, S, SO_2, SO, OCS, H_2CS, CS_2, and S_2 were detected in the coma (Le Roy et al. 2015) of 67P/Churyumov-Gerasimenko. In addition, S_3, S_4, CH_3SH, and C_2H_6S were also detected (Calmonte et al. 2016). Considering the variety of S species detected, the mean abundance of H_2S relative to H_2O remains around 1.5% (Bockelée-Morvan & Biver 2017) with values ranging from 10^{-3} to 0.1.

Protoplanetary disks are expected to strongly affect the abundance of different sulfuretted species given the multiple chemical reprocessing mechanisms at work in them. Therefore, they are key to understanding the huge differences (at a factor of a thousand) in the sulfur abundances between the diffuse ISM and dense molecular gas. Searches for S-bearing molecules in PPDs have provided few detections. Thus far, only one S species, CS, has been widely detected (Dutrey et al. 2011; Guilloteau et al. 2012, 2016; Pacheco-Vázquez et al. 2015; Podio et al. 2020a,b; Rosotti et al. 2021; Rivière-Marichalar et al. 2021; Nomura et al. 2021). We note that H_2CS was detected in MWC 480 (Le Gal et al. 2019), and H_2S was detected in GG Tau (Phuong et al. 2018) and in four protoplanetary disks in Taurus (Rivière-Marichalar et al. 2021). Furthermore, SO has been detected in a few PPDs (Pacheco-Vázquez et al. 2016; Booth et al. 2018, 2021; Le Gal et al. 2021), and SO_2 has been observed toward IRS 48 as well (Booth et al. 2021). Recently, CCS was detected toward GG Tau (Phuong et al. 2021), but the low signal-to-noise ratio (S/N) precluded the analysis of the spatial distribution. The authors could not reproduce the observed CCS column density together with other sulfuretted species, supporting the idea that astrochemical sulfur networks are incomplete. Similar problems have been encountered in CS studies, such as in the study of cold cores by Navarro-Almaida et al. (2020), where models overpredicted CS abundances by a factor of 10. Sulfur astrochemical networks have improved over the last years (Fuente et al. 2016, 2017b, 2019; Le Gal et al. 2017; Vidal et al. 2017; Laas & Caselli 2019), including new formation and destruction routes, but work is still needed to solve the issue.

The Herbig star AB Aur is a well-known Herbig A0-A1 (Hernández et al. 2004) star that hosts a transitional disk. The system is located at 162.9 pc from the Sun (Gaia Collaboration 2018), and it is perfectly suited to study the spatial distribution of gas and dust in circumstellar environments in detail. The disk extends out to a radius of 2.3″ (~373 au) in the continuum (Rivière-Marichalar et al. 2020). Molecular emission from species such as CS, $C^{18}O$, SO, H_2CO, and H_2S is observed with radii of emission peaks ranging from 0.9″ to 1.4″. The disk depicts a series of features that could be linked to planet formation, such as prominent spiral arms at the near-IR and

radio wavelengths. The system also presents a cavity in continuum emission (Piétu et al. 2005; Tang et al. 2012; Fuente et al. 2017a) that extends to ~70–100 au. Tang et al. (2012) discovered a compact source inside the cavity, which is most likely an inner disk well suited to explain the strong accretion observed toward the source (Garcia Lopez et al. 2006; Salyk et al. 2013). Rodríguez et al. (2014) detected a radio jet consistent with the high levels of accretion observed. Inside the dust cavity, prominent CO spiral arms were observed by Tang et al. (2017) using the Atacama Large Millimeter/submillimeter Array (ALMA). Other species have been detected toward AB Aur by different studies, including CO, SO, HCO$^+$, HCN, and H_2CO (Schreyer et al. 2008; Piétu et al. 2005; Tang et al. 2012, 2017; Fuente et al. 2010; Pacheco-Vázquez et al. 2015, 2016; Rivière-Marichalar et al. 2019a, 2020). The first detection of SO in a protoplanetary disk was reported, in fact, also toward AB Aur (Fuente et al. 2010; Pacheco-Vázquez et al. 2015, 2016). In Rivière-Marichalar et al. (2019a), we presented high angular resolution the NOrthern Extended Millimeter Array (NOEMA) observations of HCN and HCO$^+$, with a beam size of 0.4″. The HCO$^+$ map depicts an outer disk with decay in intensity coincident with the dust cavity, a compact source toward the center, and a bridge of material that connects the outer disk with the compact source in the center. In paper I of this series, we presented the results of a NOEMA spectral survey in AB Aur (Paper I, Rivière-Marichalar et al. 2020), where we were able to obtain zeroth-, first-, and second-moment maps, opacity maps, temperature maps, and column density maps of the transitions and species surveyed. These species included ^{12}CO, ^{13}CO, $C^{18}O$, H_2CO, and SO. We derived a mean disk temperature of 39 K, and column densities in the range 10^{12} to 5×10^{13} cm^{-2} for H_2CO, SO, HCO$^+$ and HCN, and $\sim 10^{17}$ cm^{-2} for ^{13}CO. We computed a gas-to-dust mass ratio map of AB Aur and showed it to range from 10 to 40 across the disk, with larger values close to the disk's inner edge. Such values are between two times and one order of magnitude smaller than the typical value of 100 found in the ISM. The minimum in the gas-to-dust mass ratio was coincident with the peak of the continuum emission, indicating a particularly gas-poor dust trap. We produced radially and azimuthally averaged profiles of line intensity, temperature, and column densities. Such profiles demonstrate the strong chemical segregation observed in the source, with differences as high as 100 au in the position of their peaks.

In this paper, we present the first detection of H_2S toward AB Aur obtained with NOEMA. In Sect. 2 we introduce the observations setup and summarize the reduction process. In Sect. 3 we present our results, including estimates of the H_2S column density and abundance. In Sect. 5 we discuss the implications of our results for the topic of sulfur chemistry in protoplanetary disks. Finally, in Sect. 6 we summarize our conclusions.

2. Observations and data reduction

We observed the H_2S $1_{10}-1_{01}$ transition at 168.763 GHz toward AB Aur with NOEMA between May and July 2020 using EMIR receivers (Carter et al. 2012). The source was observed for eight hours in configuration 8, with baselines ranging from 18 to 315 m. The data reduction and map synthesis was performed using GILDAS[1]/MAPPING. We used the PolyFix correlator centered at 161.5 GHz with a bandwidth of 8 GHz per sideband. A chunk with a spectral resolution of 62.5 kHz was placed at

---

[1] See http://www.iram.fr/IRAMFR/GILDAS for more information about the GILDAS software.
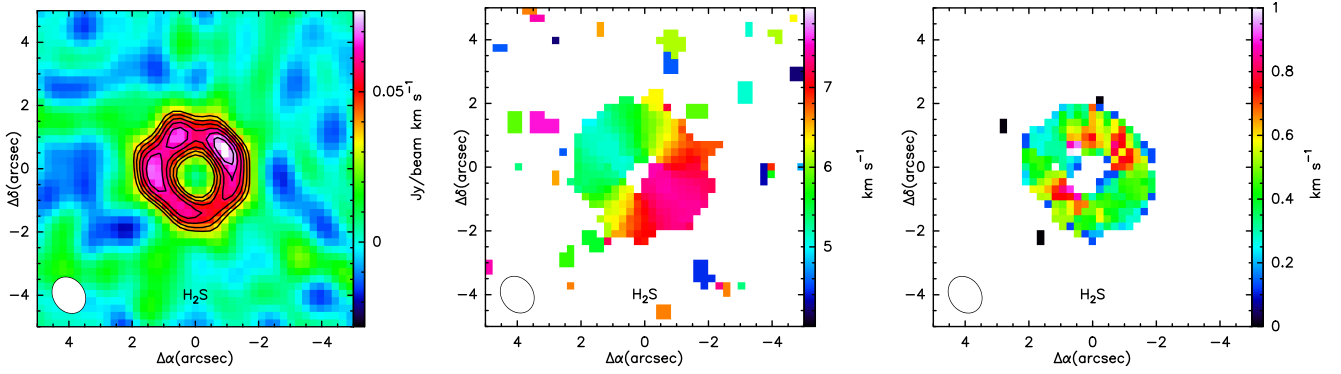
Fig. 1. *From left to right*, zeroth-, first-, and second-moment maps of the H_2S $1_{10}-1_{01}$ emission line toward AB Aur. The synthesized beam is shown in the lower left corner of each plot.
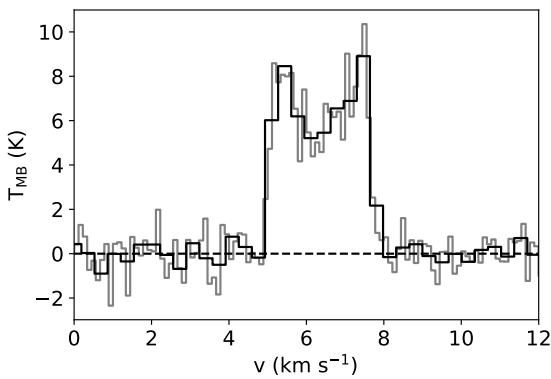

Fig. 2. Stacked H_2S $1_{01}-1_{10}$ spectrum of AB Aur inside the 5σ emission contour levels. The gray spectrum depicts the observed spectrum, and the black one depicts the same after rebinning.

168.763 GHz to observe H_2S $1_{10}-1_{01}$, reaching a velocity resolution of $0.1\,km\,s^{-1}$. The final map was built using robust weight, allowing us to reach a beam size of $1.19'' \times 0.97''$ (193 au × 158 au), with PA = 34° the PA defined as positive from N to E.

3. Results

We show in Fig. 1 the resulting zeroth-, first- and second-moment maps of H_2S $1_{10}-1_{01}$ at 168.763 GHz. The integrated intensity map depicts a ring of H_2S emission extending from $\sim 0.7''$ ($\sim$114 au) to $\sim 1.7''$ ($\sim$277 au). The ring shows strong azimuthal asymmetries, with a peak that is roughly coincident with the position of the continuum peak (Fuente et al. 2017a) and the position of the H_2CO (Rivière-Marichalar et al. 2020) and HCN (Rivière-Marichalar et al. 2019a) integrated emission peaks.

In Fig. 2 we show the stacked spectrum inside the 5σ emitting contours. The spectrum depicts the two-peaked profile characteristic of a rotating disk. The two peaks show similar intensities (8.3 and 8.8 K), and line widths (0.4 and $0.54\,km\,s^{-1}$). The blue-shifted component peaks at $5.4\,km\,s^{-1}$, and the red-shifted one at $7.0\,km\,s^{-1}$.

In Fig. 3 we show the azimuthally averaged radial profile of the H_2S $1_{10}-1_{01}$ emission line and compare it to the radial profile of other transitions that have been observed with high spatial resolution toward AB Aur, including ^{12}CO, ^{13}CO, $C^{18}O$, SO, and H_2CO (Rivière-Marichalar et al. 2020), and HCO^+ and

HCN (Rivière-Marichalar et al. 2019a). These maps have been deprojected, assuming an inclination angle $i = 26°$ and position angle PA = $-37°$. The maps were also convolved with the H_2S beam for a better comparison of the radial profiles. The H_2S emission ring shows a peak at $\sim 1.2''$ ($\sim$195 au), with emission in excess over the RMS extending from $\sim 0.51''$ ($\sim$83 au) to $\sim 2.35''$ ($\sim$383 au). The average disk width is $1.84''$ ($\sim$300 au). H_2S shows a radial profile that matches that of H_2CO. In a recent study of H_2S emission in Taurus disks, a tentative correlation between H_2S and H_2CO was shown (Rivière-Marichalar et al. 2021); our maps now point to a very similar spatial origin for both emission lines, increasing the observational support for such a correlation. Furthermore, both species have formation routes on the surface of grains. In Fig. 4 we show cuts in azimuth of the H_2S, H_2CO, $C^{18}O$, and continuum emission maps at the radius of their respective emission peaks. The similarity between H_2S and H_2CO is again prominent, with local maxima and minima at almost the same azimuths. The azimuthal contrast ratio of H_2S at the distance to the emission peak is 1.5 ± 0.3.

Assuming local thermodynamical equilibrium (LTE) we compute an H_2S column density map. Since we have observed only one o-H_2S transition ($1_{10}-1_{01}$) no rotational diagram could be computed and we thus assumed a fixed disk temperature. For consistency, we adopted a temperature of 30 K as in our previous work (Rivière-Marichalar et al. 2020), allowing the comparison between H_2S and the species surveyed in this work. The mean o-H_2S column density is $(1.5 \pm 0.3) \times 10^{13}\,cm^{-2}$, with a minimum value of $1.0 \times 10^{13}\,cm^{-2}$ and a maximum of $2.2 \times 10^{13}\,cm^{-2}$. Assuming that H_2S behaves like H_2O, we assign an ortho-to-para ratio of 3 (Hama et al. 2016), and derive a H_2S mean column density of $(1.9 \pm 0.4) \times 10^{13}\,cm^{-2}$. The resulting deconvolved column density map is shown in Fig. 5. The peak in column density is coincident with the dust trap. There are other two local maxima at PA $\sim 90°$ and $\sim 135°$.

4. Modeling the sulfur budget in AB Aur

To gain further insight into the AB Aur sulfur budget, we also computed a `Nautilus` 1D model. `Nautilus` computes the evolution of molecular abundances for a set of initial abundances and physical parameters using gas-phase, gas-grain, and surface chemistry reactions (Semenov et al. 2010; Loison et al. 2014; Wakelam et al. 2014; Reboussin et al. 2015). The parameters include gas and dust temperature, gas density, cosmic ray molecular hydrogen ionization rate ζ_{H_2}, and extinction, among others.
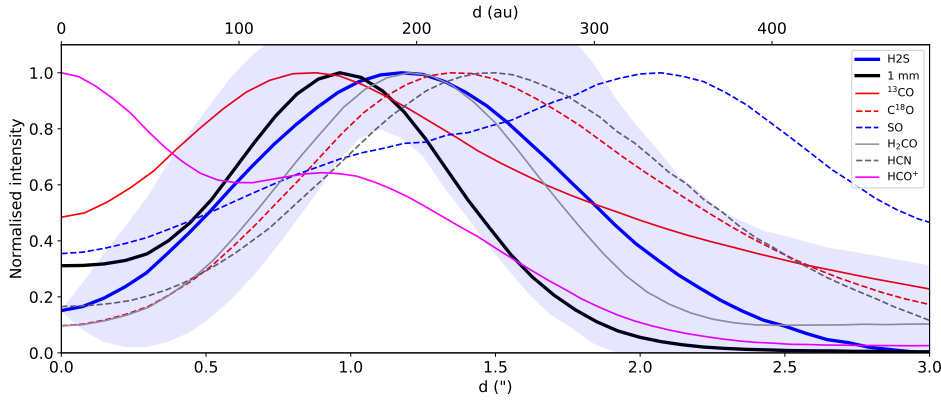
Fig. 3. H_2S azimuthally averaged radial profile compared to previous observations by this team. All the intensity maps have been convolved to match the beam size of our H_2S emission line maps. The light-blue shaded area depicts the H_2S radial profile plus or minus uncertainties.
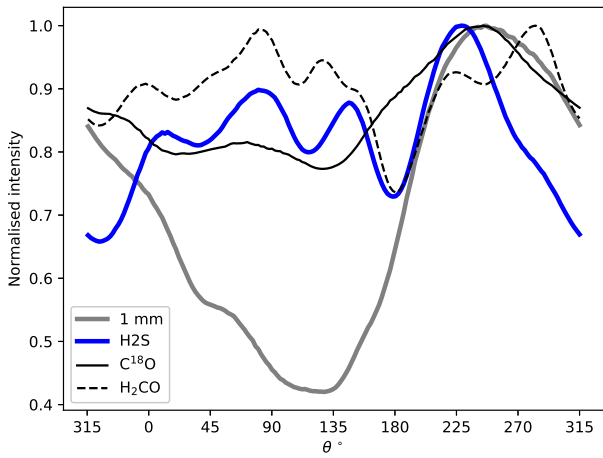

Fig. 4. H_2S azimuthal cuts compared to previous observations by this team. All the intensity maps have been convolved to match the beam size of our H_2S emission line maps. The azimuthal profiles shown were computed at the distance of the emission peak of each species. The profiles were normalized with respect to their respective peaks.
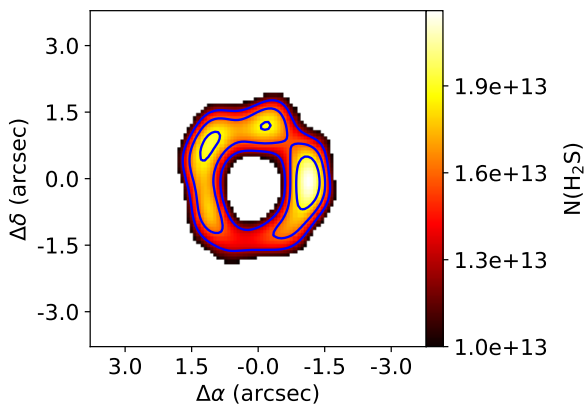
Table 1. Nautilus model input parameters for the molecular cloud prephase and the protoplanetary disk at $r = 200$ au.

Parameter	Value
Molecular cloud	
T_{gas} (K)	10
T_{dust} (K)	10
n_H	10^4
A_v	20
f_{UV} (Draine units)	1
ζ_{H_2} (s^{-1})	10^{-17}
Gas-to-dust mass ratio	100
AB Aur at $r = 200$ au	
T_{mid} (K)	39
T_{atm} (K)	65
A_v	2
f_{UV} (Draine units)	1.2×10^4
ζ_{H_2} (s^{-1})	10^{-17}
Gas-to-dust mass ratio	40

4.1. Model setup

The physical structure used in our models is the one used in Rivière-Marichalar et al. (2020), which in turn was adapted from Le Gal et al. (2019). Given the moderate resolution of the observations, we decided not to consider the radial structure and instead focus on the vertical profile at a radius of $r = 200$ au, representative of the H_2S ring described in Sect. 2. Our models included both photodesorption (with a yield of 10^{-4} molecules photon^{-1}) and chemical desorption, assuming the conditions listed in Table 1. Chemical desorption was included following the prescription by Garrod et al. (2007) for ice-coated grains implemented in Nautilus. To mimic the molecular cloud origin of the system, instead of assuming initial abundances following cosmic values, we computed a 10 K molecular cloud model and used its output abundances as the initial abundances for our 1D protoplanetary disk model. Each phase was let to evolve for 1 Myr. The input physical parameters for this model are listed in Table 1, and the initial abundances used for the molecular cloud prephase are listed in Table 2. We note that we use a nondepleted value for the sulfur abundance. Nautilus assumes a single size of 0.1 μm for the dust grains. Following Rivière-Marichalar et al. (2020), we assumed a gas-to-dust mass ratio of 40 for the AB Aur protoplanetary disk. The chemical network

Fig. 5. H_2S column density map computed assuming LTE and $T_k = 30$ K and ortho-to-para ratio of 3. The map has been deprojected assuming an inclination angle $i = 26°$ and position angle PA $= -37°$.

A refinement of the code considers grain surface and grain mantle reactions by using a three-phase structure that includes gas, grain surfaces, and grain mantles (Ruaud et al. 2016; Wakelam et al. 2017). For a more detailed description of the code see Ruaud et al. (2016) and Wakelam et al. (2017).

Table 2. Initial abundances.

Species	n_i/n_H	Reference
H$_2$	0.5	–
He	9.0×10^{-2}	1
C$^+$	1.7×10^{-4}	2
N	6.2×10^{-5}	2
O	2.4×10^{-4}	3
S$^+$	1.5×10^{-5}	4
Si$^+$	8.0×10^{-9}	4
Fe$^+$	3.0×10^{-9}	4
Na$^+$	2.0×10^{-9}	4
Mg$^+$	7.0×10^{-9}	4
P$^+$	2.0×10^{-10}	4
Cl$^+$	1.0×10^{-9}	4
F$^+$	6.7×10^{-9}	5

References. (1) Wakelam & Herbst (2008); (2) Jenkins (2009); (3) Hincelin et al. (2011); (4) Graedel et al. (1982); (5) Neufeld et al. (2015).

used is the updated version of the kida.uva.2014 (Wakelam et al. 2015) presented in Navarro-Almaida et al. (2020) which includes an enhanced chemical network for sulfur chemistry (Vidal et al. 2017). The grid consisted of 100 heights over the mid-plane with logarithmic spacing. We note that `Nautilus` is not properly suited to model the PDR-like conditions of the uppermost layers of the disk model. Diffusion between neighboring cells was not included. Since the distinction between mantle species and surface species is mostly a computational parametrization in `Nautilus`, in the following we consider grain surfaces and mantles as a single phase, called grain surface and preceded by the prefix g-, which is computed by adding up abundances in each of the solid phases (mantle and surface of grains) for each species.

For the sake of clarity, we summarize in the following the main equations describing our model. The vertical temperature profile at $r = 200$ au follows the prescription by Dartois et al. (2003) used in Rosenfeld et al. (2013), described by the following equation:

$$T(z) = \begin{cases} T_{\mathrm{mid}} + (T_{\mathrm{atm}} - T_{\mathrm{mid}}) \left[\sin\left(\frac{\pi z}{2 z_q}\right) \right]^{2\delta} & \text{if } z < z_q \\ T_{\mathrm{atm}} & \text{if } z \geq z_q, \end{cases} \tag{1}$$

where T_{atm} and T_{mid} are the temperature of the disk atmosphere and the disk mid plane at $r = 200$ au, respectively.

$$T_{\mathrm{mid}} = T_{\mathrm{mid},R_c} \left(\frac{200 \text{ au}}{R_c} \right)^{-q}, \tag{2}$$

$$T_{\mathrm{atm}} = T_{\mathrm{atm},R_c} \left(\frac{200 \text{ au}}{R_c} \right)^{-q}, \tag{3}$$

where R_c is a characteristic radius ($R_c = 98$ au, Rivière-Marichalar et al. 2020), and $z_q = 4H$, where H is the pressure scale height.

$$H = \sqrt{\frac{k_B T_{\mathrm{mid}} r^3}{\mu m_H G M_\star}}, \tag{4}$$

where k_B is the Boltzmann constant, $\mu = 2.4$ is the mean molecular weight of the gas, m_H is the proton mass, and $M_\star$ is the mass

of the central star. The mid-plane temperature T_{mid} is described by equation

$$T_{\mathrm{mid}}(r) \approx \left(\frac{\varphi L_\star}{8 \pi r^2 \sigma_{SB}} \right)^{1/4}, \tag{5}$$

where $L_\star$ is the stellar luminosity, φ is the flaring index, and σ_{SB} is the Stefan-Boltzman constant. We assumed that the dust has the same temperature as the gas. The vertical profile of the density is described by

$$\rho(z) = \rho_0 e^{-\frac{z^2}{2H^2}}, \tag{6}$$

where ρ_0 is the mid-plane density of the gas at 200 au. Finally, the UV flux at a given radius is given by equation

$$f_{UV} = \frac{0.5 f_{UV,R_c}}{\left(\frac{r}{R_c} \right)^2 + \left(\frac{4H}{R_c} \right)^2}. \tag{7}$$

4.2. Model results

In Fig. 6, we show the cumulative fraction of the total sulfur abundance for the ten most abundant sulfuretted species computed by `Nautilus` at different heights for a given radius of 200 au, where the pressure scale height H is ∼8 au. The prefix s means that the species are on the surface of dust grains. The lack of prefix means that the species are in gaseous form. The obtained distribution does not change much from $z = 0.1$ au (A_v ∼29 mag) to $z < 7$ au (A_v ∼ 11.5 mag). At these heights, most of the sulfur is in the form of H$_2$S on the surface of grains (more than 95% of the cosmic abundance at $z = 0.1$ au, and 65% at $z \sim 7$ au). At $z \sim 8$ au H$_2$S$_3$ and SO$_2$ in the surface of grains become the dominant carriers. At $z = 10$, the budget is dominated by SO$_2$ on the surface of grains (79% of the cosmic sulfur abundance). At $z = 15$ au, the budget becomes dominated by two gas species: S$^+$ and S contain 97% of the sulfur abundance. Finally, at $z = 25$ au, 99.8% is in the form of S$^+$.

The trends with the height of the different phases of the model are summarized in Fig. 7, where we represent the percentage of the sulfur cosmic abundance contained in each of the phases that are considered by the model (sulfur species in the surface of dust grains and gas-phase species) as a function of the height over the mid-plane at $r = 200$ au. As can be seen, before ∼14 au the budget is dominated by surface species. Then, around 12 au, chemical species in the gas phase start to become important sulfur carriers. At $z \sim 13$ au, the amount of sulfur in the gas phase becomes larger than the amount of sulfur locked in the surface of grains, and, at 16 au, ∼100% of the sulfur budget is contained in the gas phase.

In Fig. 8, we show the total (i.e., stacking all heights) cumulative fraction for the 10 most abundant sulfuretted species for the two stages of the model: the cold molecular cloud (top) and the AB Aur protoplanetary disk (bottom). In Table 3 we list the species that contribute to 98% of the sulfur budget in each stage of the model. As can be seen in Fig. 8, 98% of the sulfur budget in the protoplanetary disk model is contained in six species originating at different heights: g-H$_2$S, g-SO$_2$, g-H$_2$S$_3$, S$^+$, g-CS$_2$, and S. Exception made of S$^+$ and S, all of them are grain surface species. Overall, 90.5% of the sulfur content is on the surface of grains, and 9.5% is in the gas phase. As seen in Fig. 6, S$^+$ only becomes a dominant species at $z \sim 13$ au, where the temperature reaches 43 K, and the extinction is only 2.4 mag. H$_2$S is also an
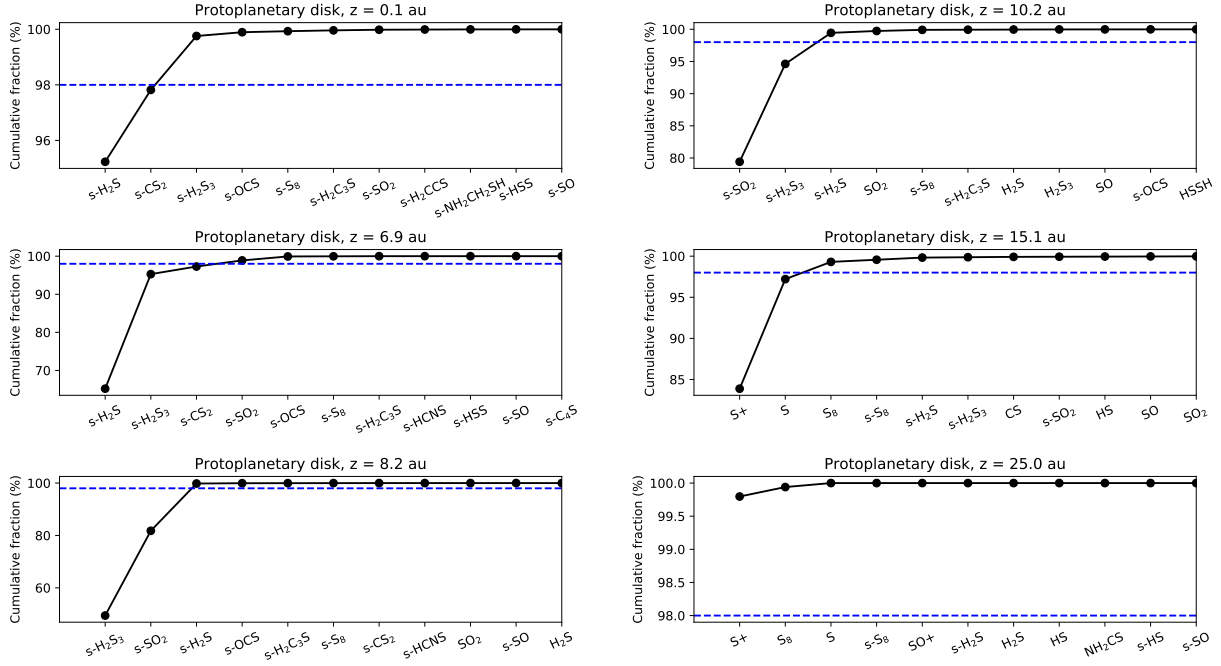
Fig. 6. Cumulative abundance fraction of sulfuretted species from `Nautilus` models at different heights above the midplane at $r = 200$ au. The horizontal blue dashed line depicts the position of the 98% cumulative fraction.
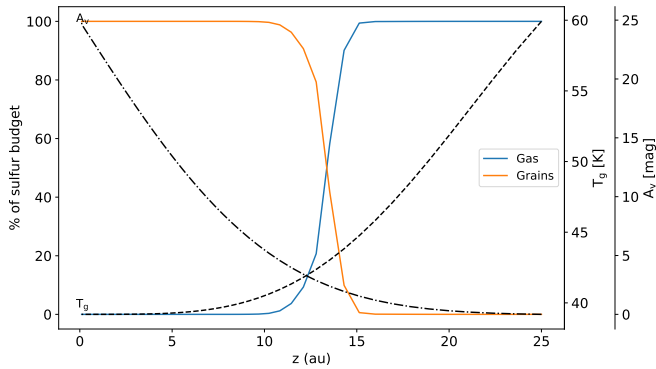

Fig. 7. Percentage of the sulfur abundance contained in the different phases of the model as a function of height at 200 au: in the mantle of grains, in the surface of grains, and in gas phase.

important sulfur carrier in the gas phase, with an abundance of 7.4×10^{-10}, compared to 9.2×10^{-6} for H_2S on the surface of grains. It becomes apparent that the main sulfur carriers are H_2S and SO_2, but they are almost fully incorporated in the surface and mantle of dust grains. H_2S in the gas phase contains only ∼0.003% of the total sulfur budget.

In Fig. 9 we show the 10 most abundant species for the different phases of the model, as well as for the global case. Surface H_2S is the third most abundant species, after g-H_2O and g-CO. Furthermore, considering all phases (Fig. 9, top left) g-H_2S is the ninth most abundant species in the model. This makes H_2S a relevant component of dust grains, whose abundance in different protoplanetary systems is worth modeling.

In Fig. 10, top panel, we show the vertical profile at $r = 200$ au of a few sulfur carriers that are important for the sulfur budget in the gas phase, namely: H_2S, CS, SO, and SO_2. This figure helps us to identify at which height over the mid-plane the emission of the different species originates. Before $z \sim 7$ au the height
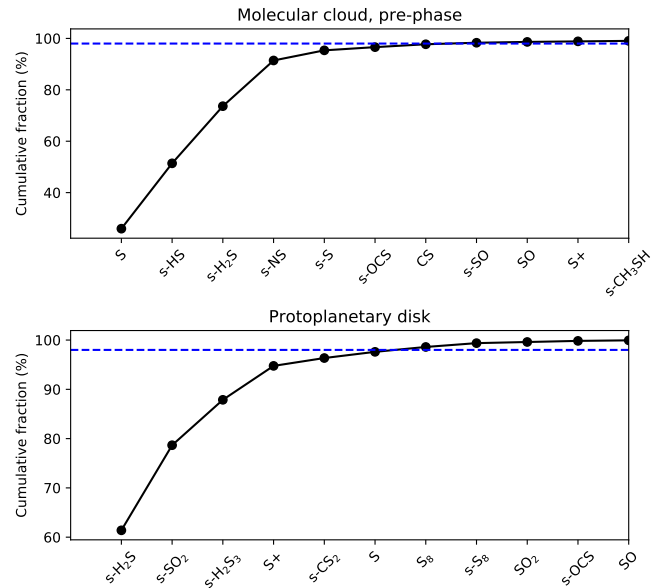

Fig. 8. Cumulative sulfur abundance fraction of the ten main sulfur carriers from `Nautilus` models. *Top*: molecular cloud. *Bottom*: AB Aur protoplanetary disk at $r = 200$ au. The horizontal blue dashed line depicts the position of the 98% cumulative fraction.

profiles of the four species remain mostly flat at low abundances. At 7 au, their abundances start to grow, and SO, and SO_2 peak around 13 au, while CS peaks at 15 au. The H_2S vertical profile forms a high abundance plateau that extends from ∼10 to ∼15 au where the abundance reaches values of a few 10^{-9}. The plateau is preceded by a dip where the abundance goes down by three orders of magnitude. In the bottom panel of Fig. 10 we show the same as in the top panel, but this time for the different phases of

Table 3. List of species that contain 98% of the sulfur budget at $r = 200$ au in our `Nautilus` model.

Species	Abundance	Fraction of total (%)
Molecular cloud		
S	3.9×10^{-6}	26.0
g-HS	3.8×10^{-6}	25.4
g-H$_2$S	3.3×10^{-6}	22.2
g-NS	2.7×10^{-6}	17.8
g-S	5.9×10^{-7}	3.9
g-OCS	1.9×10^{-7}	1.2
CS	1.7×10^{-7}	1.1
AB Aur		
g-H$_2$S	$9.2 10^{-6}$	61.4
g-SO$_2$	2.6×10^{-6}	17.3
g-H$_2$S$_3$	4.6×10^{-7}	9.2
S$^+$	1.0×10^{-6}	6.9
g-CS$_2$	1.2×10^{-7}	1.6
S	1.9×10^{-7}	1.3

Notes. The prefix g- means that the species is adsorbed in the surface of dust grains.
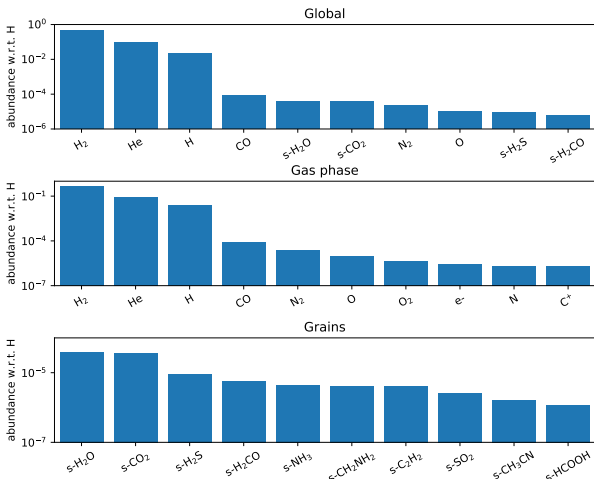
Fig. 9. Abundances of the ten most abundant species in our `Nautilus` model for the global content (*top*), the gas phase (*middle*), the surface of grains (*bottom*).

H$_2$S: gas phase and H$_2$S in the surface of grains (g-H$_2$S). At low heights over the mid-plane (high extinction), the dominant phase is H$_2$S on the surface of grains.

4.3. Parameter impact

In the following subsection, we discuss the impact of changing key model parameters on the results. The first parameter whose impact we wanted to test is the temperature of the mid-plane. To that aim, we computed a model with a mid-plane temperature of 10 K, compared to 39 K assumed in the previous model (see Table 1). The cumulative sulfur abundance fraction of the ten most relevant sulfur carriers from this model is shown in the top panel of Fig. 11. The most relevant sulfur carrier for the model

with $T_{mid} = 10$ K is g-HS, it is not in the list of the 10 most relevant sulfur carriers in the model with $T_{mid} = 39$ K. The same happens with a g-NS, which are among the most relevant sulfur carriers in the $T_{mid} = 10$ K model. Species that are important sulfur carriers in the main model ($T_{mid} = 39$ K) are irrelevant to the sulfur budget in the $T_{mid} = 10$ K model. Such species include g-SO$_2$ and g-H$_2$S$_3$. We show in the middle of Fig. 11 a comparison of the abundances of all the sulfuretted species from the model with $T_{mid} = 10$ K versus the abundances from the model with $T_{mid} = 39$ K. The figure presents a large scatter, indicating that varying the temperature of the mid-plane gas has an important impact on the derived sulfur abundances. In the bottom panel of Fig. 11 we show the abundances of a subset of important sulfur carriers. While the differences are small for H$_2$S in the surface and mantle of grains, they are large for all the other species represented. We include in the bottom panel the abundances derived from our observations assuming LTE. As can be seen, none of the models matches the two observed species, but the main model provides a good fit for H$_2$S. In the middle panel of Fig. 11 we see that some molecules show differences of several orders of magnitude. Therefore, a subset of these species can be used to get insight into the mid-plane temperature, according to models.

The second parameter that we wanted to test is the temperature of the cold cloud prephase. To that aim, we computed a model using a prephase with a temperature of 18 K. As can be seen in Fig. 12 the differences between the two models are not relevant, and a change in the prephase gas temperature will produce almost the same results, especially in the gas phase.

We also tested the impact of a varying grain size distribution. To that aim, we assumed a different grain size at each height, with 1 mm grains in the mid-plane, 0.1 μm in the atmosphere, and a logarithmic interpolation in between. We use the same dust temperature in both models. We show in Fig. 13 the results from this model versus the original model results. While the difference is not as large as when changing the mid-plane temperature, the impact of grain sizes cannot be ignored. As can be seen in the top panel of Fig. 13, the species that dominate the sulfur budget are similar to those in the case of the original model (Fig. 8). However, although the grain size distribution affects the results, those for the gaseous species tracked in the bottom panel of Fig. 13 remain mostly unchanged.

Finally, we tested the impact of the UV field by computing a model with a meager value of the scale factor of the UV flux, $f_{UV} = 12$, compared to $f_{UV} = 12 \times 10^4$ in the main model (see Table 1). We show in Fig. 14 a comparison between the two models. The impact on the abundances is small, and only a few species show a difference larger than one order of magnitude. One of those species is S$^+$, which drops by more than one order of magnitude when a low UV flux is assumed.

5. Discussion

The detection of H$_2$S emission in a ring around AB Aur is the second resolved observation of H$_2$S in a protoplanetary disk, after the detection toward GG Tau by Phuong et al. (2018), and the sixth detection after the four single dish detections in Taurus protoplanetary disk (Rivière-Marichalar et al. 2021).

Assuming LTE we derived a mean column density of $(1.9 \pm 0.4) \times 10^{13}$ cm^{-2} and a mean abundance with respect to ^{13}CO of $(1.5 \pm 0.4) \times 10^{-4}$. By assuming ^{12}CO/^{13}CO $= 60$, and X(^{12}CO) $= 10^{-4}$, we converted the abundance with respect
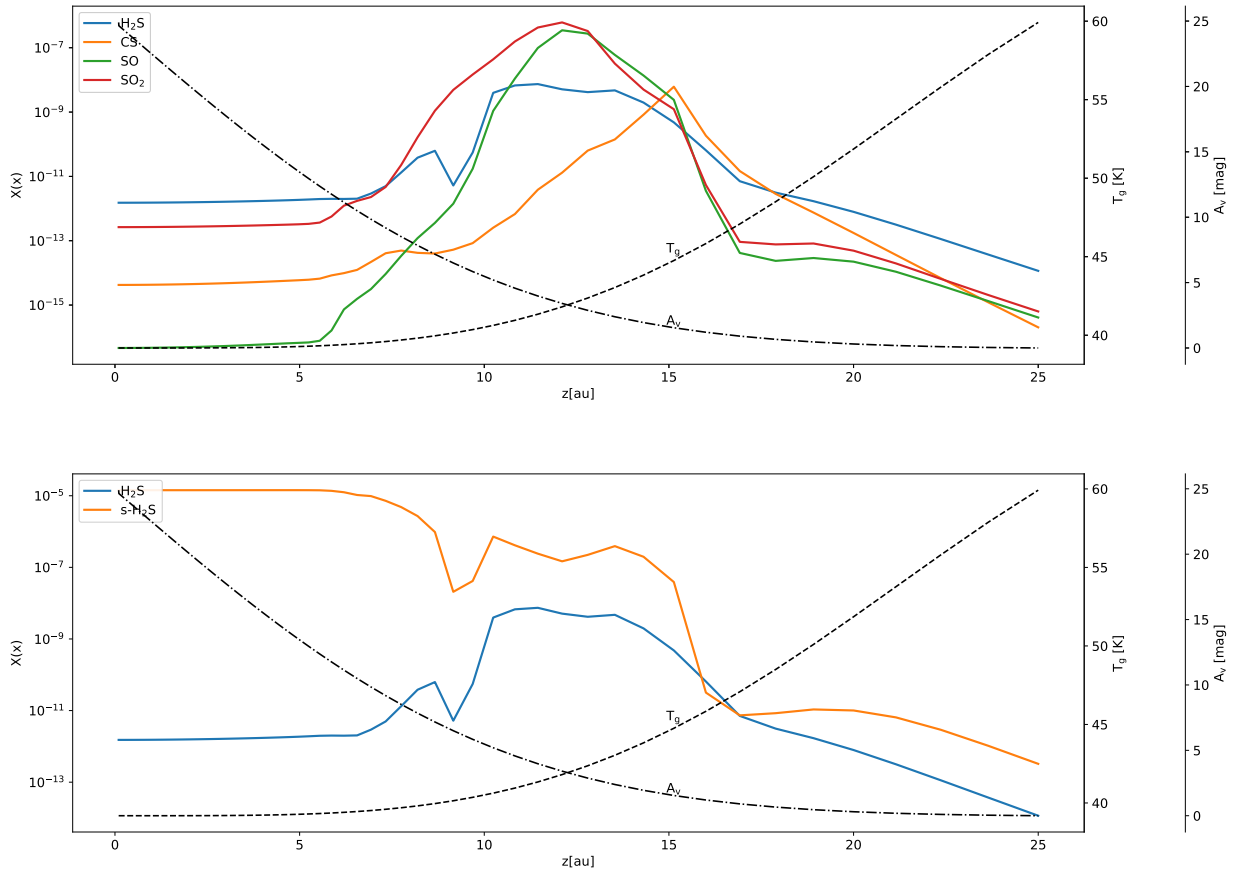
Fig. 10. Vertical profiles at $r = 200$ au. *Top*: of important sulfur carriers in the gas phase, namely H_2S, CS, SO, and SO_2. *Bottom*: of H_2S in the gas phase and in the surface of grains (g-).We also include the vertical profile of A_v and T_g for comparison.

Table 4. Comparison of abundances in different environments.

Species	AB Aur	GG Tau	Horsehead PDR	TMC 1-CP	Orion KL
H_2S	2.4×10^{-10}	$1.8 \times 10^{-10(*)}$	3.3×10^{-10}	1.1×10^{-9}	1.5×10^{-6}
SO	3.2×10^{-9}	–	3.9×10^{-10}	1.0×10^{-9}	8×10^{-8}
CS	$2.6 \times 10^{-10(*)}$	$3.1 \times 10^{-10(*)}$	4.5×10^{-10}	1.3×10^{-8}	7×10^{-8}
S budget	$>9.2 \times 10^{-10}$	$>4.9 \times 10^{-10}$	$>1.2 \times 10^{-9}$	$>1.5 \times 10^{-8}$	$>1.7 \times 10^{-6}$
S budget$^{(\dagger)}$	–	–	1.5×10^{-9}	–	1.9×10^{-6}

Notes. [*]: Assuming $^{12}CO/^{13}CO = 60$ and $X(^{12}CO) = 10^{-4}$. [†]: Including other S-bearing species.
References. GG Tau: Phuong et al. (2018); Horsehead PDR: Rivière-Marichalar et al. (2019b); TMC 1-CP: Rodríguez-Baras et al. (2021); Navarro-Almaida et al. (2020); Orion-KL: Tercero et al. (2010); Esplugues et al. (2014); Crockett et al. (2014).

to ^{13}CO to an abundance with respect to H_2, resulting in a mean value of $(2.4 \pm 0.6) \times 10^{-10}$. The region surrounding the dust trap depicts the maximum H_2S abundance in the disk. Our `Nautilus` 1D model from Sect. 4 predicts $N(H_2S) = 3.5 \times 10^{13}$ $(X(H_2S) = 7.5 \times 10^{-10})$, about two times larger than the value that we estimate assuming LTE. Using the same methodology, we derived the SO column density from our SO 5_6–4_5 NOEMA observations from Rivière-Marichalar et al. (2020), resulting in a mean SO column density of 1.0×10^{14} cm^{-2}, resulting in a mean abundance of 3.2×10^{-9}, ~2.4 times smaller than the value predicted by our `Nautilus` model, $N(SO) = 7.8 \times 10^{14}$ $(X(SO) = 9.8 \times 10^{-9})$. Recently, CCS was detected toward GG

Tau (Phuong et al. 2021). The authors could not simultaneously reproduce the observed column density of CCS and other sulfuretted species, supporting the idea that astrochemical sulfur networks are incomplete. The complexity of simultaneously predicting the abundance of important sulfur carriers such as CS, SO, SO_2, and H_2S is a known issue of sulfur chemistry networks in astrochemical models (Navarro-Almaida et al. 2020). Sulfur astrochemical networks have improved over the last years (Le Gal et al. 2017; Vidal et al. 2017; Navarro-Almaida et al. 2020), with new formation and destruction routes. Yet, progress is needed to solve the issue. However, the goal of the model is not to reproduce the observed values, but rather to get insight into
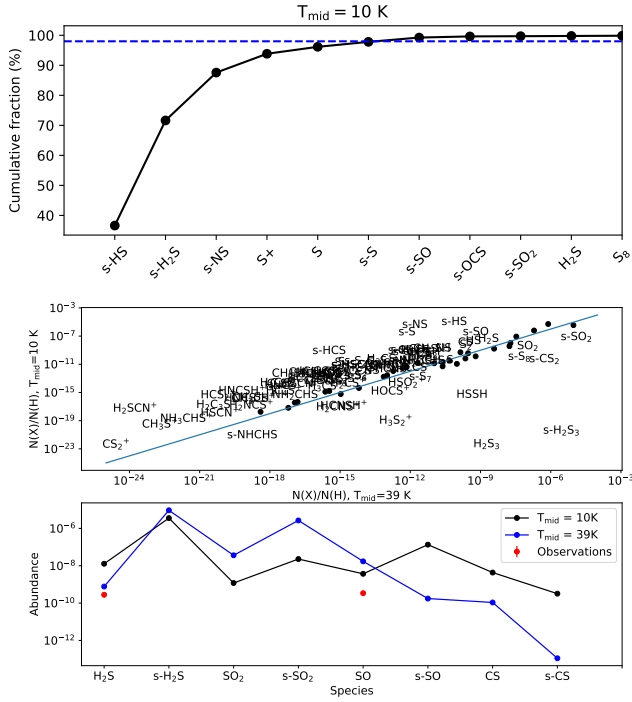
Fig. 11. Impact of varying the mid-plane temperature on the model results. *Top*: cumulative sulfur abundance fraction of the ten main sulfur carriers for the `Nautilus` model with T_{mid} = 10 K. *Middle*: abundance of sulfuretted species computed assuming T_{mid} = 10 K versus the abundance computed assuming T_{mid} = 39 K. We show the names of the species when there is an order of magnitude difference between both models, and plot black dots otherwise. *Bottom*: abundance of a subset of the most relevant sulfur carriers for the two mid-plane temperatures used.
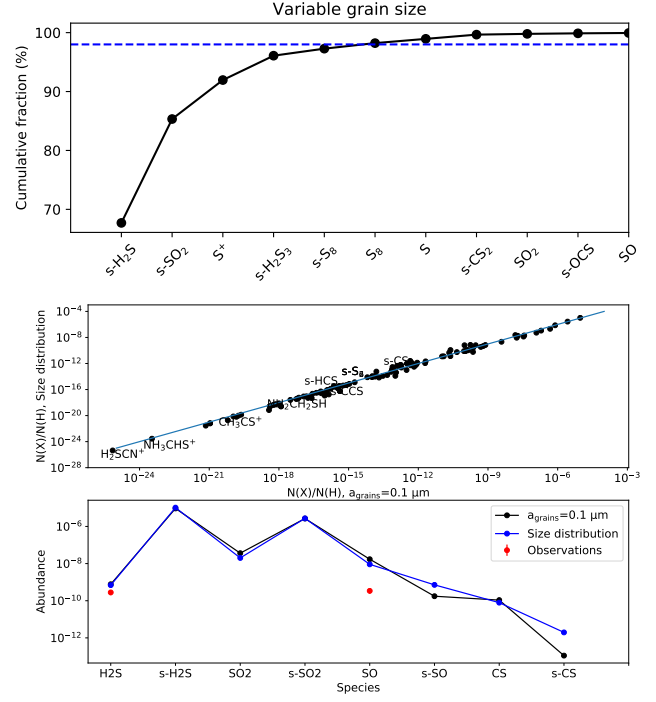

Fig. 13. Impact of varying grain size on the model results. *Top*: cumulative sulfur abundance fraction of the ten main sulfur carriers for the `Nautilus` model computed assuming a grain size distribution. *Middle*: abundance of sulfuretted species computed assuming a_{grains} = 0.1 μm versus the abundance computed assuming a grain size distribution. We show the names of the species when there is an order of magnitude difference between both models, and plot black dots otherwise. *Bottom*: abundance of a subset of the most relevant sulfur carriers for the model with fixed grain size and with a distribution of sizes.
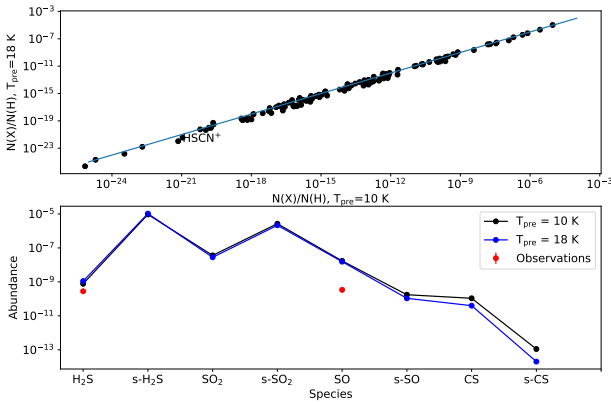

Fig. 12. Impact of varying the prephase temperature on the model results. *Top*: abundance of sulfuretted species computed assuming T_{gas} = 10 K versus the abundance computed assuming T_{gas} = 18 K for the molecular cloud prephase. *Bottom*: abundance of a subset of the most relevant sulfur carriers for the two prephase temperatures used.
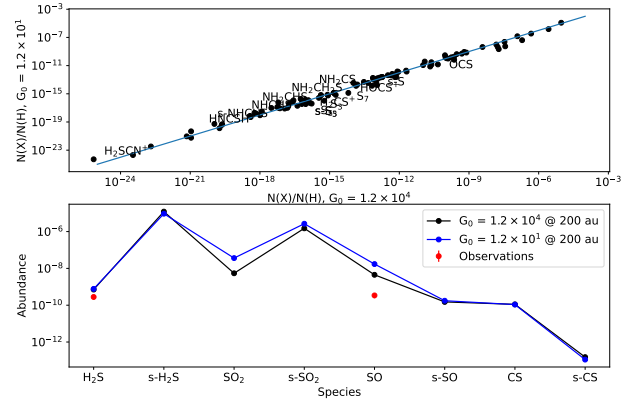

Fig. 14. Impact of varying the UV flux on the model results. *Top*: the abundance of sulfuretted species computed assuming f_{UV}=12 Draine unit versus the abundance computed assuming f_{UV} = 1.2×10⁴ Draine units. *Bottom*: the abundance of a subset of the most relevant sulfur carriers for the a model with f_{UV} = 12 Draine unit and with f_{UV} = 1.2×10⁴ Draine units.

the main sulfur carriers. Furthermore, considering the uncertainties in the model, related to the physical structure and the details of the chemical network, we consider that the model results in a good fit of the H$_2$S line.

From the computed column density map we derived a mean H$_2$S abundance with respect to ^{13}CO of $(1.5 \pm 0.4) \times 10^{-4}$. Assuming a ^{12}CO abundance of 10^{-4} and ^{12}CO/^{13}CO = 60,

we derived a mean abundance with respect to H nuclei X(H$_2$S) = $(2.4 \pm 0.6) \times 10^{-10}$. To help us with the discussion we also derived abundances for SO, the other sulfuretted species that we observed toward AB Aur (Rivière-Marichalar et al. 2020). The mean SO abundance with respect to ^{13}CO is $(1.9 \pm 0.2) \times 10^{-3}$, resulting in an abundance with respect to H nuclei X(SO) = $(3.1 \pm 2.3) \times 10^{-9}$.

In the following, we compare the H2S abundance derived 2 in AB Aur with that derived in different environments (see Table 4). Phuong et al. (2018) used `Nautilus` to derive a column density for the disk around the M0 star GG Tau $N(H_2S) = 3.4 \times 10^{13}$ cm^{-2}, close to our estimate for AB Aur. Rivière-Marichalar et al. (2021) detected H$_2$S in four young stellar objects in Taurus, with column densities in the range 3.2×10^{12} cm^{-2} to 1.9×10^{13} cm^{-2}. This set of values was computed for a disk with an outer radius of 500 au. However, this size is larger than the H$_2$S disk observed toward AB Aur. If an outer radius of 250 au is assumed, the computed column densities are in the range 10^{13} cm^{-2} to 7×10^{13} cm^{-2}, close to the value derived for AB Aur. The difference in spectral type does not impact the individual column densities. Since H$_2$S has been detected only in a few protoplanetary disks, no statistical trend can be derived, but the proximity between observed abundances is interesting.

The abundance derived for AB Aur is four orders of magnitude lower than that found in the Orion KL hot core (1.5×10^{-6}, Esplugues et al. 2014), but similar to that found in two PDRs, the Horsehead nebula (3.1×10^{-10}, Rivière-Marichalar et al. 2019a) and the Orion Bar (4.0×10^{-10}, Leurini et al. 2006). This is particularly interesting because H$_2$S presents almost the same abundance in very different PDRs (the Horsehead with a radiation intensity of $G_0 \sim 10^2$ and the Orion Bar, a much more extreme PDR with $G_0 = 10^4$). Overall, the chemical abundances in PDRs are governed by the ratio of the UV radiation field and the density (G_0/n_H). In the case of H2S, this species is mainly formed on grain surfaces and later released into the gas phase through photodesorption in regions dominated by high UV radiation (Jiménez-Escobar & Muñoz Caro 2011; Jiménez-Escobar et al. 2014; Fuente et al. 2017a). The high UV radiation is also responsible for the destruction of H$_2$S through dissociation processes. The interplay between formation and destruction mechanisms makes the position of the H$_2$S abundance peak roughly independent of G_0. This is partially confirmed by our experiment with a low-UV model, which results in very close H$_2$S abundances: 6.9×10^{-10} for the model with a low UV field versus 7.5×10^{-10} for the model with high UV field.

Regarding density, it has a crucial role in the H$_2$S abundance, since both the formation of solid H$_2$S on the surface of grains and its desorption depend on the density of the region. In particular, solid H$_2$S is mainly formed through recombination of S$^+$ ions (formed as the UV photons penetrate the gas ionizing S atoms) with negatively charged grains followed by desorption. Adsorption of S$^+$ is favored in dense regions by the increased collision rates between gas-phase species and grains (Gail & Sedlmayr 1975; Bel et al. 1989; Ruffle et al. 1999; Druard & Wakelam 2012). Once that solid H$_2$S is formed, the H$_2$S photodesorption rates depend on the grain size distribution, which in turn depends on n_H. This implies that, for a given radiation field, the H$_2$S abundance peak will be shifted toward the densest part of a PDR as theoretically found by Goicoechea et al. (2021).

The huge change in the abundance of H$_2$S in the gas phase from hot cores to Class II disks and PDRs points to H$_2$S being an important sulfur carrier in the icy surface of dust grains, such that it is almost fully evaporated in hot cores, thus increasing the fraction of gas-phase H$_2$S. This is confirmed by our `Nautilus` model from Sect. 4, where only $\sim$0.0001% of H$_2$S is in gas phase. In this model, a large fraction ($\sim$61%) of the cosmic sulfur abundance is locked in the surface and mantle of grains in the form of H$_2$S, and another 17% is also locked in the surface and mantle of

grains in the form of SO$_2$. The low sulfur abundances observed in AB Aur and other protoplanetary disks (Le Gal et al. 2019) can indeed be explained if sulfur is locked in the ice surface of dust grains, similar to what happens in dense cores (Millar & Herbst 1990; Ruffle et al. 1999; Vidal et al. 2017; Laas & Caselli 2019). Laas & Caselli (2019), using a chemical network with 860 species, showed that most sulfur is locked on dust grains and that grain chemistry could account for the depleted sulfur in molecular clouds. Our 1D protoplanetary disk model shows a similar result, with most of the sulfur locked in the surface of dust grains in the form of H$_2$S, SO$_2$ and H$_2$S$_3$ at high extinctions, and dominated by S$^+$ at low extinctions.

We note that our results for the sulfur budget depend on the chemical network used, as well as on the details of the model. For instance, in the molecular cloud model by Laas & Caselli (2019) the amount of H$_2$S in ices is negligible for most of the cloud's life. The chemical network used in Laas & Caselli (2019) is different from the one we used in the present paper, and their model does not include a mantle phase, which results in very different abundances of H$_2$S on the surface of grains. We highlight, however, that H$_2$S is the most abundant sulfuretted species in comets (Bockelée-Morvan & Biver 2017), in agreement with our results.

Cazaux et al. (2022) find that, under efficient self-shielding conditions, H$_2$S survives on the surface of grains as the ice below 100 K, and is largely depleted from the grains at 150 K. However, if no self-shielding is assumed, most H$_2$S is transformed, under the influence of UV radiation, into S$_x$ sulfur chains. Our `Nautilus` model predicts that gaseous S$_8$ and that the surface of grains is the seventh and eighth major sulfur carrier.

6. Summary and conclusions

In this study we present resolved observations of H$_2$S $1_{01}-1_{10}$ in AB Aur. This is only the second time that H$_2$S has been resolved in a protoplanetary disk, and the sixth global detection. The main results from our study can be summarized as follows:

1. We detected o-H$_2$S $1_{01}-1_{10}$ in a ring extending from $\sim$0.67$''$ ($\sim$109 au) to 1.69$''$ ($\sim$275 au). We observed strong azimuthal asymmetries. The position of the peak coincides with the position of the continuum and C^{18}O emission peaks. The radial profile of the emission overlaps with that of H$_2$CO.

2. Assuming LTE, we estimated a mean column density of $(1.9 \pm 0.4) \times 10^{13}$ cm^{-2}. Making simple assumptions, we translated this column density into an abundance of $(2.4 \pm 0.6) \times 10^{-10}$.

3. A `Nautilus` 1D model shows that most (99.99%) of the H$_2$S is locked in the surface of dust grains. The model also shows that they are the main sulfur carriers. Our model further shows that $\sim$90.5% of the sulfur is locked on the surface of grains, and only 9.5% of it is available in the gas phase.

Our study of the sulfur budget in the protoplanetary disk surrounding AB Aur points to H$_2$S being the most important sulfur carrier on the surface of grains. Furthermore, it is the third most abundant species on the surface of grains, after H$_2$O and CO$_2$. Our results probe that H$_2$S observations are an essential diagnostic to determine the sulfur depletion in protoplanetary disks. Observations of H$_2$S and other sulfuretted species toward more young stellar objects are needed to understand sulfur depletion and put our observations of AB Aur in context.

References

Asplund, M., Grevesse, N., Sauval, A. J., & Scott, P. 2009, ARA&A, 47, 481
Balsiger, H., Altwegg, K., Bochsler, P., et al. 2007, Space Sci. Rev., 128, 745
Bel, N., Lafon, J. P. J., Viala, Y. P., & Loireleux, E. 1989, A&A, 208, 331
Biver, N., Moreno, R., Bockelée-Morvan, D., et al. 2016, A&A, 589, A78
Bockelée-Morvan, D., & Biver, N. 2017, Philos. Trans. R. Soc. London Ser. A, 375, 20160252
Boissier, J., Bockelée-Morvan, D., Biver, N., et al. 2007, A&A, 475, 1131
Boogert, A. C. A., Schutte, W. A., Helmich, F. P., Tielens, A. G. G. M., & Wooden, D. H. 1997, A&A, 317, 929
Booth, A. S., Walsh, C., Kama, M., et al. 2018, A&A, 611, A16
Booth, A. S., van der Marel, N., Leemker, M., van Dishoeck, E. F., & Ohashi, S. 2021, A&A, 651, L6
Calmonte, U., Altwegg, K., Balsiger, H., et al. 2016, MNRAS, 462, S253
Carter, M., Lazareff, B., Maier, D., et al. 2012, A&A, 538, A89
Cazaux, S., Carrascosa, H., Muñoz Caro, G. M., et al. 2022, A&A, 657, A100
Crockett, N. R., Bergin, E. A., Neill, J. L., et al. 2014, ApJ, 787, 112
Daflon, S., Cunha, K., de la Reza, R., Holtzman, J., & Chiappini, C. 2009, AJ, 138, 1577
Dartois, E., Dutrey, A., & Guilloteau, S. 2003, A&A, 399, 773
Druard, C., & Wakelam, V. 2012, MNRAS, 426, 354
Dutrey, A., Wakelam, V., Boehler, Y., et al. 2011, A&A, 535, A104
Esplugues, G. B., Viti, S., Goicoechea, J. R., & Cernicharo, J. 2014, A&A, 567, A95
Fuente, A., Cernicharo, J., Agúndez, M., et al. 2010, A&A, 524, A19
Fuente, A., Cernicharo, J., Roueff, E., et al. 2016, A&A, 593, A94
Fuente, A., Baruteau, C., Neri, R., et al. 2017a, ApJ, 846, L3
Fuente, A., Goicoechea, J. R., Pety, J., et al. 2017b, ApJ, 851, L49
Fuente, A., Navarro, D. G., Caselli, P., et al. 2019, A&A, 624, A105
Gaia Collaboration 2018, VizieR Online Data Catalog: I/345
Gail, H. P., & Sedlmayr, E. 1975, A&A, 41, 359
Garcia Lopez, R., Natta, A., Testi, L., & Habart, E. 2006, A&A, 459, 837
Garrod, R. T., Wakelam, V., & Herbst, E. 2007, A&A, 467, 1103
Geballe, T. R., Baas, F., Greenberg, J. M., & Schutte, W. 1985, A&A, 146, L6
Goicoechea, J. R., & Cuadrado, S. 2021, A&A, 647, L7
Goicoechea, J. R., Pety, J., Gerin, M., et al. 2006, A&A, 456, 565
Goicoechea, J. R., Aguado, A., Cuadrado, S., et al. 2021, A&A, 647, A10
Graedel, T. E., Langer, W. D., & Frerking, M. A. 1982, ApJS, 48, 321
Guilloteau, S., Dutrey, A., Wakelam, V., et al. 2012, A&A, 548, A70
Guilloteau, S., Reboussin, L., Dutrey, A., et al. 2016, A&A, 592, A124
Hama, T., Kouchi, A., & Watanabe, N. 2016, Science, 351, 65
Hernández, J., Calvet, N., Briceño, C., Hartmann, L., & Berlind, P. 2004, AJ, 127, 1682
Hily-Blant, P., Pineau des Forêts, G., Faure, A., & Lique, F. 2022, A&A, 658, A168
Hincelin, U., Wakelam, V., Hersant, F., et al. 2011, A&A, 530, A61
Howk, J. C., Sembach, K. R., & Savage, B. D. 2006, ApJ, 637, 333
Jenkins, E. B. 2009, ApJ, 700, 1299
Jiménez-Escobar, A., & Muñoz Caro, G. M. 2011, A&A, 536, A91
Jiménez-Escobar, A., Muñoz Caro, G. M., & Chen, Y. J. 2014, MNRAS, 443, 343
Laas, J. C., & Caselli, P. 2019, A&A, 624, A108
Le Gal, R., Herbst, E., Dufour, G., et al. 2017, A&A, 605, A88
Le Gal, R., Öberg, K. I., Loomis, R. A., Pegues, J., & Bergner, J. B. 2019, ApJ, 876, 72
Le Gal, R., Öberg, K. I., Teague, R., et al. 2021, ApJS, 257, 12
Le Roy, L., Altwegg, K., Balsiger, H., et al. 2015, A&A, 583, A1
Leurini, S., Rolffs, R., Thorwirth, S., et al. 2006, A&A, 454, L47
Loison, J.-C., Wakelam, V., Hickson, K. M., Bergeat, A., & Mereau, R. 2014, MNRAS, 437, 930
Millar, T. J., & Herbst, E. 1990, A&A, 231, 466
Mumma, M. J., & Charnley, S. B. 2011, ARA&A, 49, 471
Navarro-Almaida, D., Le Gal, R., Fuente, A., et al. 2020, A&A, 637, A39
Neufeld, D. A., Godard, B., Gerin, M., et al. 2015, A&A, 577, A49
Nomura, H., Tsukagoshi, T., Kawabe, R., et al. 2021, ApJ, 914, 113
Pacheco-Vázquez, S., Fuente, A., Agúndez, M., et al. 2015, A&A, 578, A81
Pacheco-Vázquez, S., Fuente, A., Baruteau, C., et al. 2016, A&A, 589, A60
Palumbo, M. E., Tielens, A. G. G. M., & Tokunaga, A. T. 1995, ApJ, 449, 674
Phuong, N. T., Chapillon, E., Majumdar, L., et al. 2018, A&A, 616, L5
Phuong, N. T., Dutrey, A., Chapillon, E., et al. 2021, A&A, 653, L5
Piétu, V., Guilloteau, S., & Dutrey, A. 2005, A&A, 443, 945
Podio, L., Garufi, A., Codella, C., et al. 2020a, A&A, 642, L7
Podio, L., Garufi, A., Codella, C., et al. 2020b, A&A, 644, A119
Reboussin, L., Wakelam, V., Guilloteau, S., Hersant, F., & Dutrey, A. 2015, A&A, 579, A82
Rivière-Marichalar, P., Fuente, A., Baruteau, C., et al. 2019a, ApJ, 879, L14
Rivière-Marichalar, P., Fuente, A., Goicoechea, J. R., et al. 2019b, A&A, 628, A16
Rivière-Marichalar, P., Fuente, A., Le Gal, R., et al. 2020, A&A, 642, A32
Rivière-Marichalar, P., Fuente, A., Le Gal, R., et al. 2021, A&A, 652, A46
Rodríguez, L. F., Zapata, L. A., Dzib, S. A., et al. 2014, ApJ, 793, L21
Rodríguez-Baras, M., Fuente, A., Riviére-Marichalar, P., et al. 2021, A&A, 648, A120
Rosenfeld, K. A., Andrews, S. M., Wilner, D. J., Kastner, J. H., & McClure, M. K. 2013, ApJ, 775, 136
Rosotti, G. P., Ilee, J. D., Facchini, S., et al. 2021, MNRAS, 501, 3427
Ruaud, M., Wakelam, V., & Hersant, F. 2016, MNRAS, 459, 3756
Ruffle, D. P., Hartquist, T. W., Caselli, P., & Williams, D. A. 1999, MNRAS, 306, 691
Salyk, C., Herczeg, G. J., Brown, J. M., et al. 2013, ApJ, 769, 21
Schreyer, K., Guilloteau, S., Semenov, D., et al. 2008, A&A, 491, 821
Semenov, D., Hersant, F., Wakelam, V., et al. 2010, A&A, 522, A42
Tang, Y. W., Guilloteau, S., Piétu, V., et al. 2012, A&A, 547, A84
Tang, Y.-W., Guilloteau, S., Dutrey, A., et al. 2017, ApJ, 840, 32
Tercero, B., Cernicharo, J., Pardo, J. R., & Goicoechea, J. R. 2010, A&A, 517, A96
Tieftrunk, A., Pineau des Forets, G., Schilke, P., & Walmsley, C. M. 1994, A&A, 289, 579
Vastel, C., Quénard, D., Le Gal, R., et al. 2018, MNRAS, 478, 5514
Vidal, T. H. G., Loison, J.-C., Jaziri, A. Y., et al. 2017, MNRAS, 469, 435
Wakelam, V., & Herbst, E. 2008, ApJ, 680, 371
Wakelam, V., Castets, A., Ceccarelli, C., et al. 2004, A&A, 413, 609
Wakelam, V., Vastel, C., Aikawa, Y., et al. 2014, MNRAS, 445, 2854
Wakelam, V., Loison, J. C., Herbst, E., et al. 2015, ApJS, 217, 20
Wakelam, V., Loison, J. C., Mereau, R., & Ruaud, M. 2017, Mol. Astrophys., 6, 22